Supplement of Solid Earth, 17, 947–977, 2026
https://doi.org/10.5194/se-17-947-2026-supplement

Solid Earth
Open Access

Supplement of

From strong plates to weak boundaries: strain localization in the lithospheric mantle with low- to high-temperature dislocation creep

Etienne Van Broeck et al.

Correspondence to: Etienne Van Broeck (etienne.van-broeck@umontpellier.fr) and Fanny Garel (fanny.garel@umontpellier.fr)

Contents

S1 Finite-element mesh and additional resolution tests

The adapted finite-element mesh is shown in Fig. S1 at transition (t_{tr}) and localization times (t_{PB}) for the reference localizing simulation ***ref-1***. In this simulation, the minimum and the maximum element size are 1 km and 5 km (z $<$ 100 km) to 100 km (z $\geq$ 100 km) , respectively. The mesh automatically adapts on the following criteria: temperature (5 K), velocity ($3{\cdot}10^{-11}$ m s^{-1}), second invariant strain rate (log$_{10}$ scale - 0.01) and viscosity (log$_{10}$ scale - 0.01). The latter two criteria are evidenced by the small element size (i) in the mid-lithosphere around 900 K where the vertical viscosity variation is large (Fig. 9 and C1 in the main text), (ii) next to the central incipient plate boundary, and (iii) in the regions where the asthenospheric mantle flow changes orientation (cf Fig. 3 of the main text).

We perform resolutions tests keeping the same adaptivity criteria, but varying the minimum element sizes: 2000, 1000, 500,

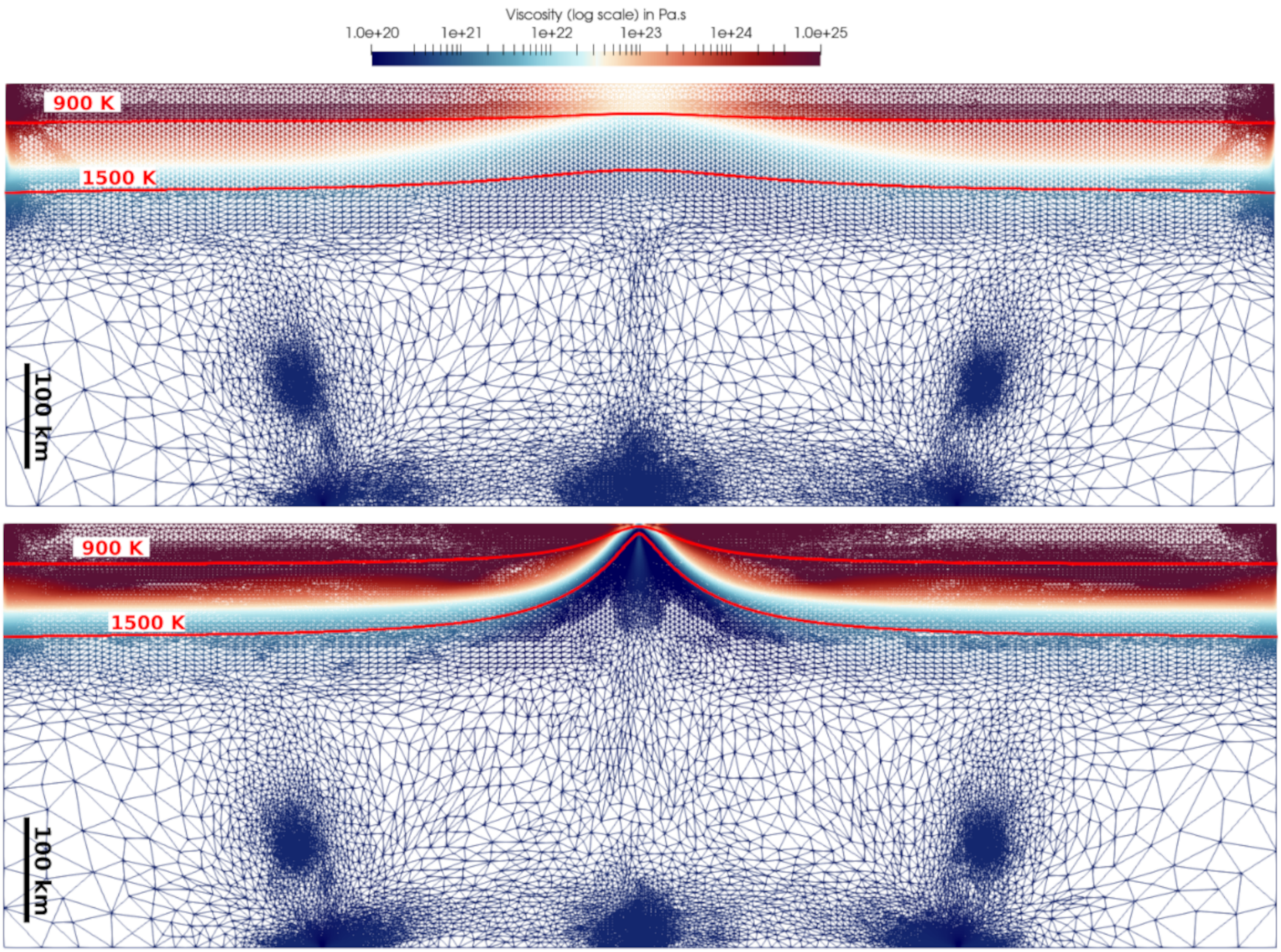

Figure S1. Finite-element mesh of the whole simulation domain (1200×400 km) superimposed on the viscosity field for Simulation ***ref-1*** (rheology $D - d_{\text{LT-HT}} - Y_{500\,\text{MPa}}$, initial plate age of 50 Myrs, extension rate $v_{1/2}$ of 1 cm/yr), shown at the transition time t_{tr} =6.5 Myr (top), and at the time t_{PB} =12 Myr when the plate boundary becomes steady (bottom), corresponding to snapshots of velocity and deformation fields in Fig. 3b in the main text.

200 or 100 m. For rheology $D - d_{\text{LT-HT}} - Y_{500\,\text{MPa}}$, deformation localization is only slightly faster for smaller minimum edge

lengths (Fig. S2a), with less than 1.5 Myr difference when the element size is 200 m rather than 1000 m. Thus, we choose 1000 m for minimum element size for most simulations in this study, i.e. a compromise between computation times and accuracy of model predictions.

For a rheology with yield-stress restricted to low temperatures ($D-d-Y^{900/950K}_{\text{200/500 MPa}}$), there is on the contrary a large difference between 1000 and 500 m minimum size (Fig. S2b). In this simulation, the thin high-viscosity layer at the transition between creep and yielding domain, which is only a few kilometers thick (Fig. 9a,c and C1-c in the main text), cannot be well-resolved with a minimum size of 1000 m: we thus perform simulations with such rheology with a minimum element size of 200 m to ensure that the slow localization (described in Section 4.3 of the main text) is not mesh-dependent.

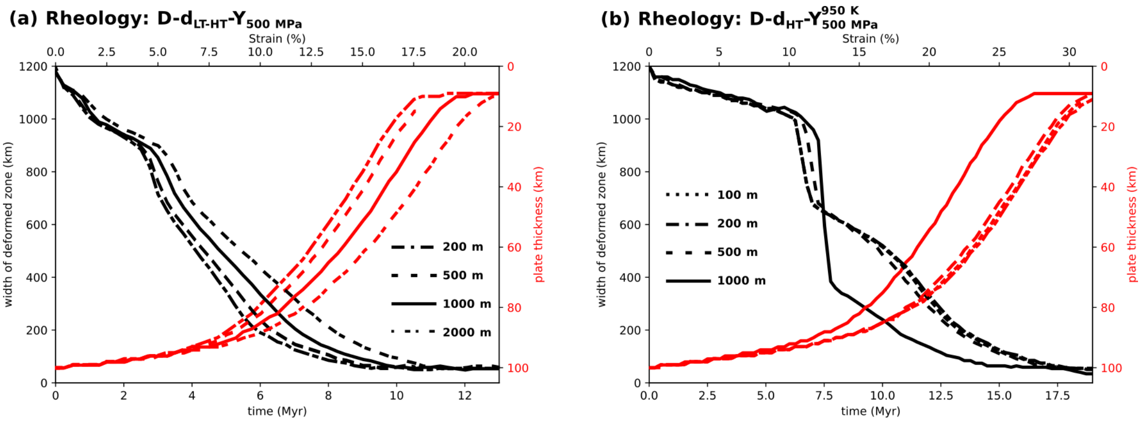

Figure S2. Influence of the mesh minimum element size on the evolution of the width of the deformed zone $w(t)$ (black lines) and of plate thickness h_{plate} at the domain center (red lines) in the reference setup (half-spreading rate $v_{1/2}$ of 1 cm yr^{-1} and initial plate age equal to 50 Myr). (a) Rheology $D-d_{\text{LT-HT}}-Y_{\text{500 MPa}}$ combining diffusion creep, low- and high-temperature dislocation creep and a yield stress of 500 MPa. For minimum element mesh size of 200; 500 or 1000 m, transition and incipient plate boundary times (t$_{tr}$ and t$_{PB}$) are 6 and 10.5 Myr; 6 and 10.75 Myr or 6.5 and 12 Myr, respectively. (b) Rheology $D-d_{HT}-Y^{950\ K}_{500\ MPa}$ combining diffusion creep, high-temperature dislocation creep and a yield stress of 500 MPa restricted to temperatures lower than 950 K. For minimum element mesh size of 100; 200; 500 or 1000 m, transition and localization times (t$_{tr}$ and t$_{PB}$) are of 12.5 and 19 Myr; 12.5 and 19 Myr; 11.75 and 18.5 Myr or 8 and 16 Myr, respectively.

S2 Boundary conditions

S2.1 Main simulations: details of 1-D Couette outflow at domain side boundaries

We compute a theoretical velocity profile $u_x(z)$ for a 1-D Couette flow

- with the half extension velocity $v_{1/2}$ at the top and a null velocity at the bottom,
- for a vertical viscosity profile associated to diffusion creep viscosity for a 50 Myr-old plate.

The simulation domain of thickness H (400 km) is discretized into 400 constant-viscosity layers, which, assuming incompressible Stokes equations in each layer i

$$\frac{d^2\ u_x^i}{d\ z^2} = 0 \tag{S1}$$

leads to a linear velocity profile $u_x^i(z) = a_i z + b_i$. The constant shear stress τ_{xz} is equal to $a_i\eta_i$ with:

$$\tau_{xz}\ =\ -\eta_i \frac{d\ u_x}{d\ z} \tag{S2}$$

The continuity of horizontal velocity and shear stress at each interface between layers, combined with the top ($u_x(0) = v_{1/2}$) and bottom ($u_x(H) = 0$) boundary conditions, leads to a well-posed linear system, whose solution yields the vertical profile of horizontal velocity ($u_x(z)$).
This exact profile u_x is then approximated to simplify input outflow velocity profile at the domain sides $v_x(z)$:

$$v_x(z) = \begin{cases} v_{1/2}(1 - \frac{z}{z_{\mathrm{LAB}}}) + V(z_{\mathrm{LAB}})\frac{z}{z_{\mathrm{LAB}}} & \text{for } z \leq z_{\mathrm{LAB}} \\ V(z) & \text{for } z > z_{\mathrm{LAB}}, \end{cases} \tag{S3}$$

where z_{LAB} is the depth of 'constant-velocity' plate, defined following Garel and Thoraval (2021) as the depth where the horizontal velocity drops below 99 % of the surface extension velocity $v_{1/2}$, e.g. $z_{\mathrm{LAB}} = 89$ km for a 50 Myr-old plate ('Couette age'). $V(z)$ is a 10th-order polynomial fit of $u_x(z)$, ensuring the continuity of the velocity profile at $z = z_{LAB}$ (Fig. S4):

$$V(z) = c_{10} \cdot z^{10} + \cdots + c_1 \cdot z + c_0 \tag{S4}$$

with coefficients c_j given in Table S1 for $v_{1/2} = 1$ cm yr^{-1}.

Table S1. Polynomial coefficients c_j of vertical velocity profile imposed as sides boundary conditions, calculated for $v_{1/2} = 1$ cm yr^{-1} and a 'Couette' age of 50 Myr. For other extension velocities, coefficients c_j are increased or decreased proportionally to the velocity ratio.

c_{10}	c_9	c_8	c_7	c_6	c_5
1.62607080 10^{-63}	-4.53868567 10^{-57}	5.60944110 10^{-51}	-4.03504583 10^{-45}	1.86626092 10^{-39}	-5.77967776 10^{-34}
c_4	c_3	c_2	c_1	c_0	
1.20780239 10^{-28}	-1.66874438 10^{-23}	1.43959164 10^{-18}	-6.94070902 10^{-14}	1.73487485 10^{-9}	

S2.2 Main simulations: details of bottom boundary conditions

At the domain bottom boundary, a purely vertical inflow (v_x=0) is prescribed over a 600-km wide region centered at x = 600 km ($300 \leq$ x ≤ 900 km). Within this central segment, the vertical velocity $v_z(x)$, that adjusts to side boundary conditions and free-surface deformation, is rather steady, with a central peak around $\sim$1 cm yr^{-1} for $v_{1/2}$=1 cm yr^{-1} (Fig. S7). Outside this central segment, a no-slip and closed condition is imposed with $v_x = v_z = 0$. The inflow lateral restriction ensures that strain localization develops preferentially at the domain center (Sect. S2.3) without the need for an initial heterogeneity in the lithosphere — e.g. weak seed (Huismans and Beaumont, 2007; Tetreault and Buiter, 2018), or thermal perturbation (Brune et al., 2012; Heckenbach et al., 2021).

S2.3 Additional tests varying (steady) bottom and side boundary conditions

We perform a suite of additional simulations ensuring the robustness of our results, by varying the kinematic boundary conditions along vertical sides and/or the box bottom (Fig.S3 and S4b).
In this study, we compare various combinations of mantle rheology. Yet, the 1-D Couette outflow is calculated for a vertical viscosity profile depending solely on a diffusion creep flow law (Eq. 1 in the main text, and Sect. S2.1). However, including dislocation creep is expected to emphasize the below-plate weakening (e.g. Patočka et al., 2024). Thus, we further evaluate whether the vertical structure of the imposed velocity profile influences the results obtained for Simulation *Ref-1* (rheology $D - d_{LT-HT} - Y_{500\,\mathrm{MPa}}$:

- a 1-D Couette profile imposed at the vertical sides computed from a viscosity profile featuring a subplate low-viscosity layer mimicking a 'below-plate weakening' (Fig. S4; Fig.S3b).
- a vertically-uniform extension rate over a 400-km thickness, imposed along the vertical sides of the simulation box (Fig.S3c),

– a free-slip and closed boundary imposed at the box bottom, along with a vertically-uniform 'plate' extension rate imposed between 0 and 89 km depth combined with a purely free horizontal velocity ($v_z = 0$) between 89 and 400 km depths (Fig.S3d).

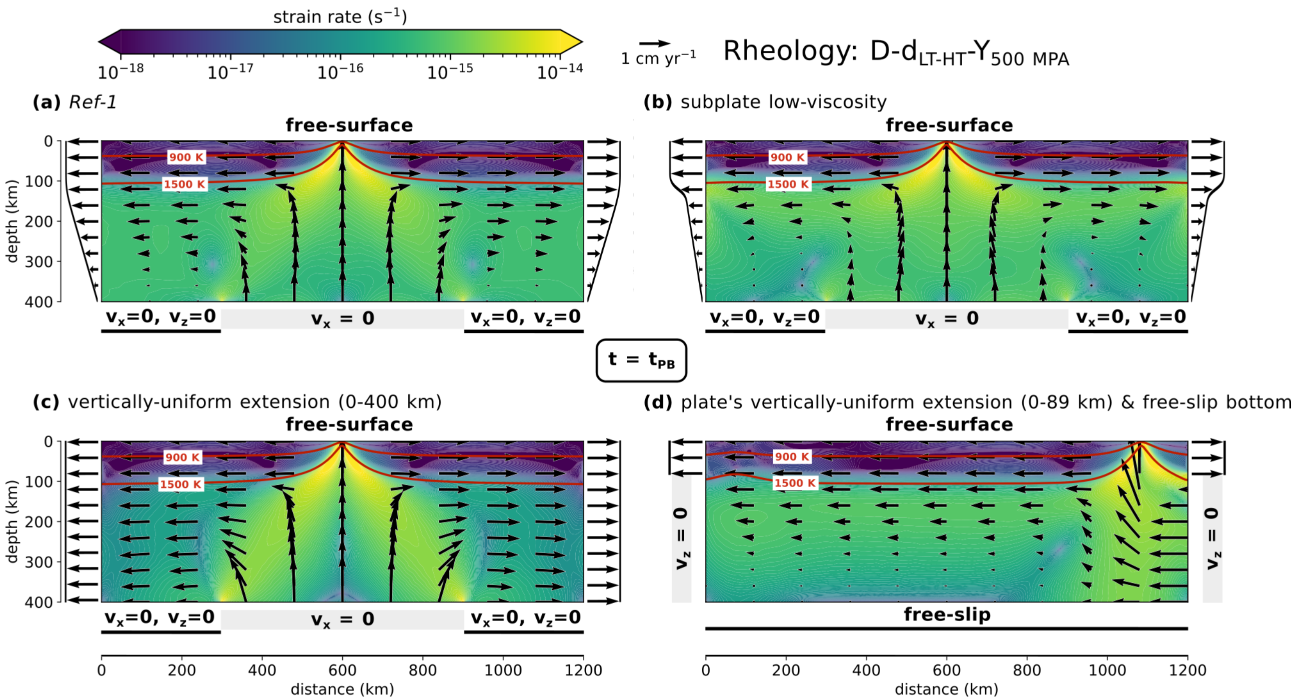

Figure S3. Flow patterns and strain rate field at t_{PB} (i.e. $\approx$ 12 Myr, Fig.S5) for simulations performed with different kinematic boundary conditions : (a) Simulation ***ref-1*** ; (b) subplate low-viscosity layer; (c) vertically-uniform extension velocity; and (d) constant outflow 'plate' velocity with a free-slip imposed along the closed bottom. All simulations feature rheology $D - d_{LT-HT} - Y_{500MPa}$ for an initial thermal plate age of 50 Myr and a half extension rate $v_{1/2} = 1$ cm yr^{-1}. The background field represent the second invariant of the strain rate, the red lines represent the 900 and 1500 K isotherms. Black vectors depict the velocity field.

The overall scenarios of localization are similar to the one obtained for Simulation ref-1, with only a short delay in deformation localization (< 1.5 Myr, at t_{PB}) for the simulation with a sub-plate low-viscosity (Fig. S5). We also note that the simulation with bottom free-slip boundary conditions differs only in the location of plate-boundary formation (Fig. S3d), which occurs closer to the side of the domain and not at its center. These tests suggest that the chosen boundary conditions do not narrow the range of extensional scenarios that are obtained. In addition, in all the numerical experiments described in the main text, the prescribed velocity at the lateral boundaries is calculated for a 'Couette age' of 50 Myr, even if the actual initial thermal age of the simulation is different (e.g. 10 Myr or 100 Myr). Because the thermal structure of the lithosphere evolves with time, the Couette velocity profile computed for a given 'Couette age' may not strictly correspond to the evolving thermal state of the model. We therefore perform sensitivity tests to assess the impact of using a single 'Couette age' (50 Myr): two 1-D Couette profiles are computed from a diffusion-creep calculated with a 'Couette age' corresponding to the initial thermal age of 10 Myr or 100 Myr (Fig. S4; Fig. S6). Varying the kinematics boundary conditions as a function of the 'Couette' age or the initial thermal age does not significantly alter the localization scenarios described in the main text: simulations featuring an initial 'thermal age' of 10 Myr and 100 Myr exhibit a slightly faster localization (~0.5 Myr) for higher 'Couette ages' (50 and 100 Myr in Fig. S6a and b, respectively). We conclude that our results do not depends on the chosen 'Couette age', that is why we choose a 'Couette age' of 50 Myr for the prescribed kinematic boundary conditions at the side boundaries of all our simulations. This choice facilitates direct comparison between simulations for equivalent extension rates.

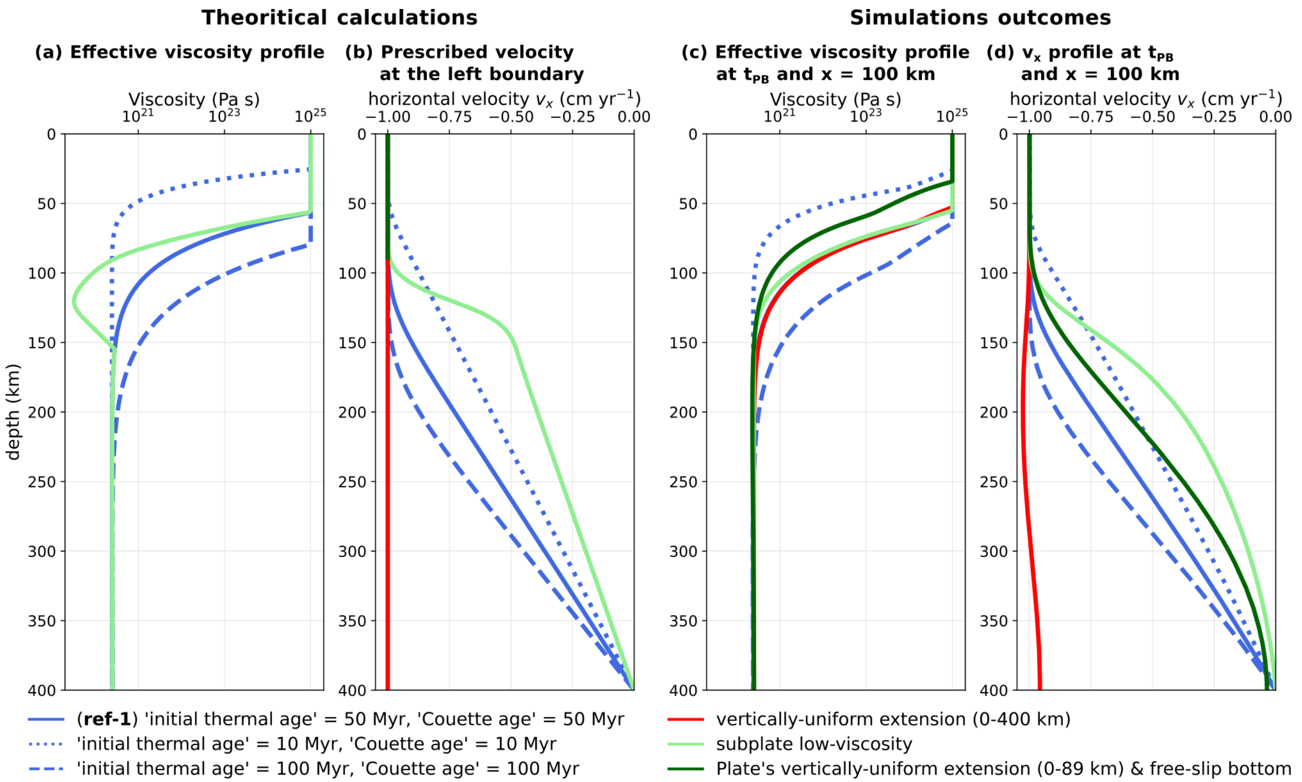

Figure S4. (a, b) Theoritical vertical profiles of viscosity and horizontal velocity for different - side - boundary conditions. (a) Viscosity profiles calculated using a diffusion creep rheology for plate ages of 10, 50 and 100 Myr (blue curves). The 'below-plate' weakening (lightgreen curve) corresponds to the diffusion creep viscosity profile which is gradually weakened up to 20 times at 100 km depth. (b) The prescribed velocity at the left hand side of the domain (the right hand boundary is symmetrical) is calculated from the corresponding viscosity profile (panel 'a'). The red curve is a uniform velocity with depth, the velocity profile in dark green is prescribed up to a 89 km depth only. (c, d) Outcomes of the simulations: profiles of effective viscosity (panel c), and of horizontal velocity (panel d) for rheology $D-d_{LT-HT}-Y_{500MPa}$ at time t_{PB} and at the position x = 100 km (i.e. 100 km away from the left side).

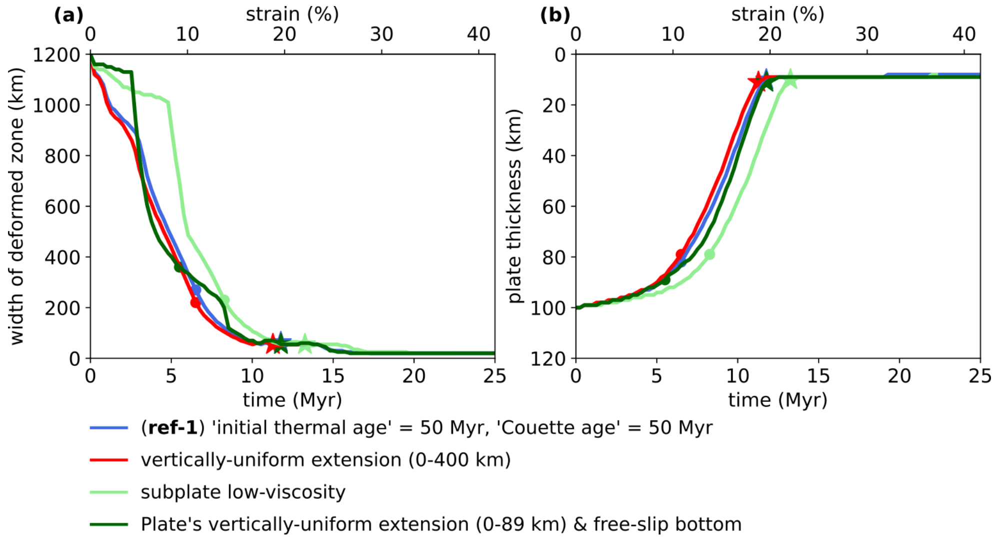

Figure S5. Evolution with time (and cumulated strain) of (a) width of the enhanced deformation zone w, and (b) plate thickness h_{plate} at $x = 600$ km for simulations performed with the same rheology ($D - d_{LT-HT} - Y_{500\,\mathrm{MPa}}$), initial ('thermal') plate age (50 Myr), and extension velocity ($v_{1/2}$ = 1 cm yr^{-1}). Only the boundary conditions differ between the simulations. The times t_{tr} and t_{PB} are denoted by points and stars, respectively.

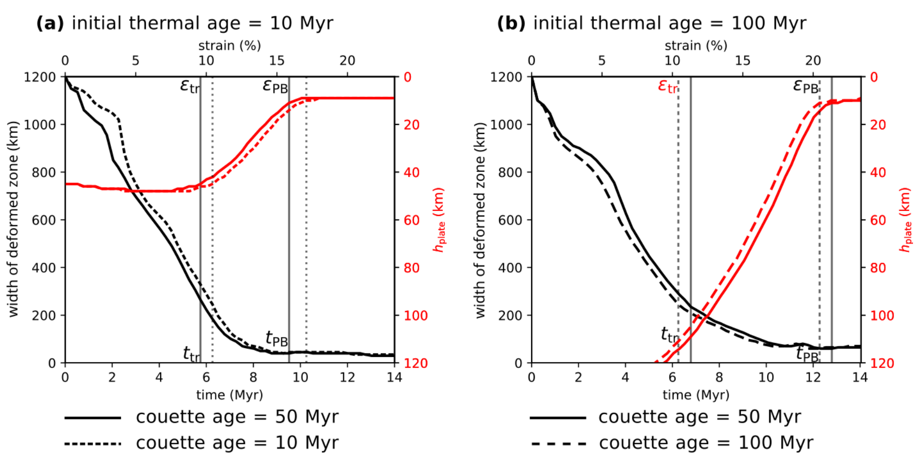

Figure S6. Evolution of the width of deformed zone (black), and of the plate thickness h_{plate} (red) for $v_{1/2}$=1 cm yr^{-1}, for initial 'thermal' plate ages of 10 Myr (a) or 100 Myr (b). Dashed and solid compare results for 'Couette' ages (boundary condition of the lateral velocity profiles) either identical to the thermal age, or of 50 Myr.

S2.4 Additional test: enhancing bottom inflow

We perform one simulation in which the bottom inflow is enhanced by imposing $v_z(x)$ in a simulation with the same rheology, initial plate age and lateral spreading as in Simulation *ref-1*. The forced bottom vertical inflow is calculated to balance the total side horizontal outflow, which is twice the integral of the horizontal velocity profile $v_x(z)$:

$$\int_{\frac{L}{2}-\frac{L_f}{2}}^{\frac{L}{2}+\frac{L_f}{2}} v_z(x)\,dx = 2\int_0^H v_x(z)\,dz \tag{S5}$$

with L the total domain width (1200 km), L_f the width of the bottom segment with no-null v_z. We assume a parabolic velocity inflow at the bottom boundary between $\frac{L}{2}-\frac{L_f}{2}$ and $\frac{L}{2}+\frac{L_f}{2}$ peaking at $v_{\text{z-max}}$:

$$v_z(x) = a\left(x-\frac{L}{2}\right)^2 + v_{\text{z-max}} \tag{S6}$$

with coefficient $a = -\frac{4}{(L_f)^2}v_{\text{z-max}}$. L_f is calculated as:

$$L_f = \frac{3}{v_{\text{z-max}}}\int_0^H v_x(z)\,dz \tag{S7}$$

The simulation with enhanced vertical inflow features a bottom peak velocity $v_{\text{z-max}}$ = 6 cm yr^{-1} with $L_f \sim 130$ km width (Fig. S7). We observe a faster strain localization under this enhanced inflow (Fig S8a), with a shorter Stage 1 (transition time

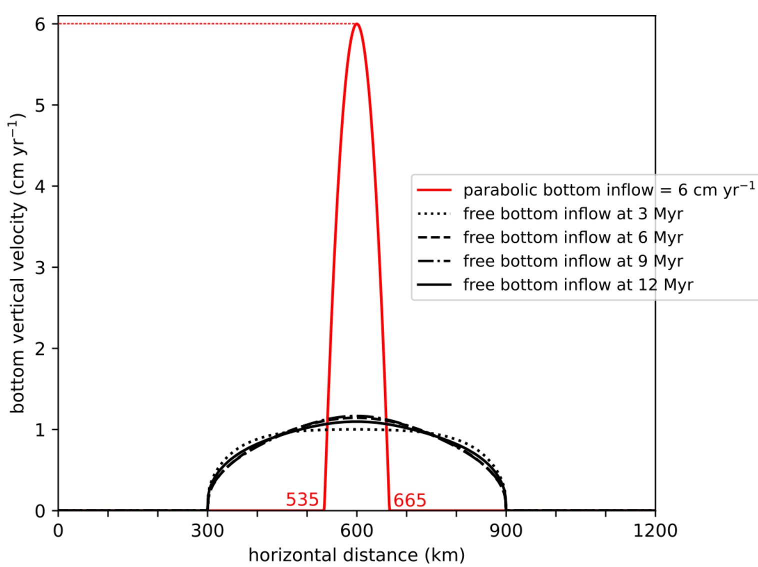

Figure S7. Output vertical velocity along domain bottom boundary (z = 400 km) at different times during Simulation ***ref-1*** (black lines), and input parabolic 'enhanced' inflow as bottom boundary condition for the additional simulation (red line).

$t_{\text{tr}} = 4.8$ vs 6.5 Myr, associated to a faster narrowing rate) and a comparable Stage 2 duration (localization time $t_{\text{PB}} = 9.8$ vs. 11.8 Myr, i.e., less than 0.5 Myr difference when removing the shift in Stage 1 duration). The enhanced asthenosphere upwelling results in a higher strain rate at the box center, hence a slightly higher mechanical weakening ($F_{\text{SR}} \geq 60$ % in the dislocation creep domain in Stage 1 compared to $F_{\text{SR}} \geq 50$ % in Simulation *ref-1*, Fig. S8b). This simulation is a first-order proxy for lithosphere deformation ahead of a plume arrival: increasing the vertical mantle inflow leads to stronger weakening and faster strain localization, even without introducing a thermal anomaly or melt weakening.

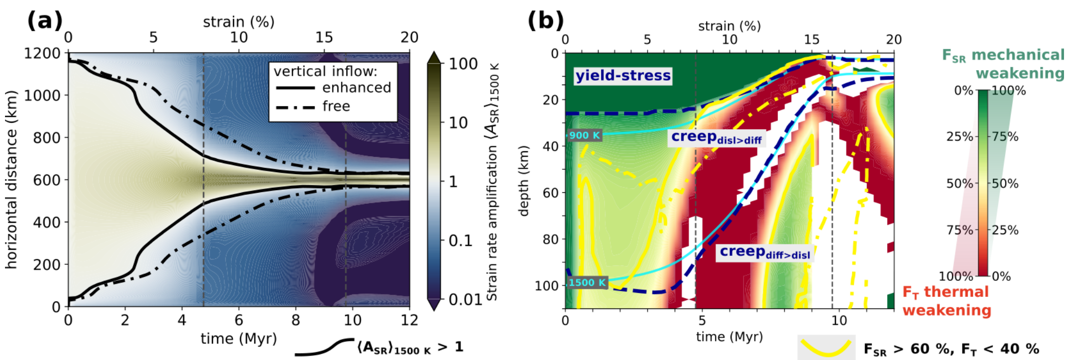

Figure S8. Evolution of (a) vertically-averaged strain rate amplification and (b) relative contributions to weakening F_{T} and F_{SR} computed at $x = 600$ km for the simulation with an enhanced vertical inflow peaking at 6 cm yr^{-1}. Dash-dotted contour refers to Simulation *ref-1* in panels (a- strain-rate amplification equal to 1 and (b - threshold of 60 % mechanical weakening).

S3 Rheology

S3.1 Comparing dynamic and lithostatic pressures

The amplitude of dynamic pressure is high in the cold lithosphere and decreases with time (∼-500 MPa, Fig. S9). The largest differences compared to the lithostatic pressure are located in the shallow cold and yielding part of the lithosphere which is not pressure dependent (Eq. 8 in the main text). At greater depth, where deformation is dominated by creep mechanisms, the lithostatic pressure is equivalent to the total pressure, and the dynamic pressure is negligible.

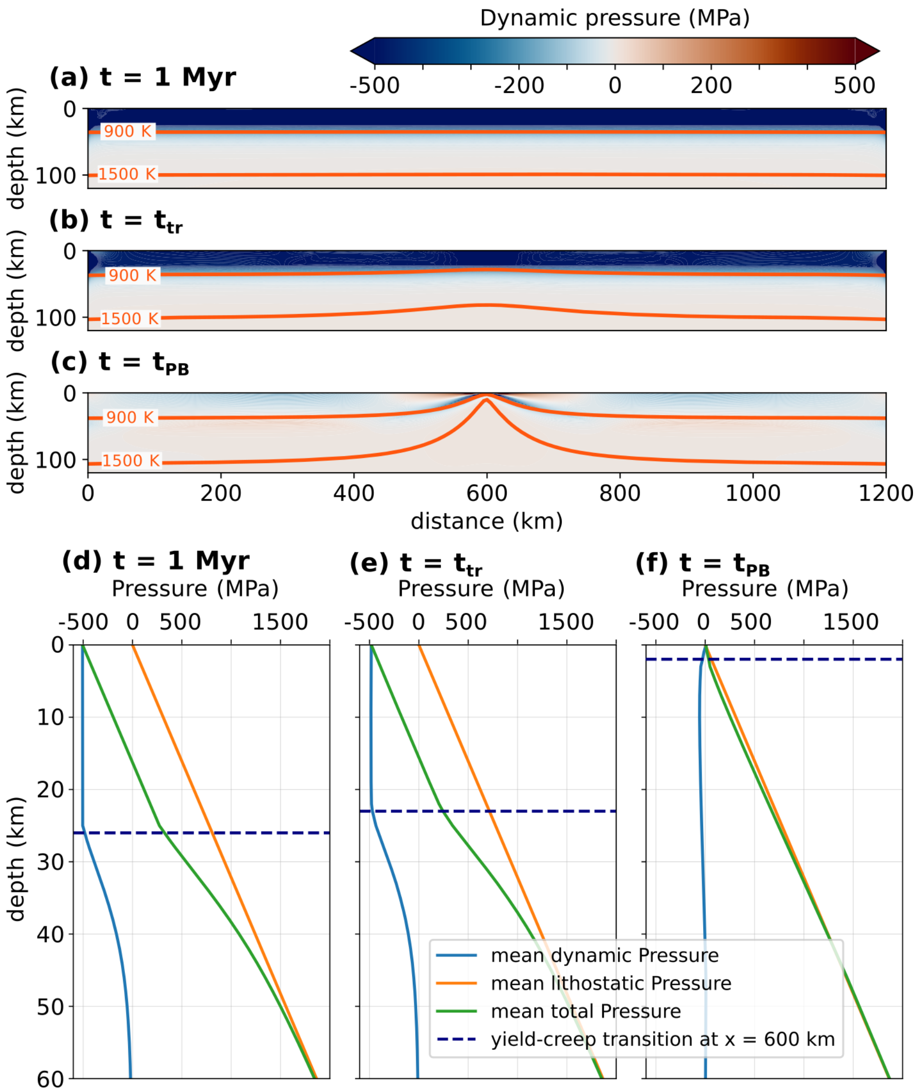

Figure S9. Simulation Ref-1 at three different times: 1 Myr, t_{tr} and t_{PB}. (a-c) cross-section of dynamic pressure over 120 km depth. (d-f) Pressure as a function of depth, the blue, orange and green curves represent the mean value for the dynamic, lithostatic and total (dynamic + lithostatic) pressure, respectively. The yield-creep transition depth at x = 600 km is reported with darkblue dashed line on each graphs

S3.2 Ensuring the consistency of deformation partitioning between diffusion and dislocation creeps with iterative computation of creep viscosity

When both diffusion creep and dislocation creep (HT or LT-HT) are included in the rheological parameterization, the effective creep viscosity is computed as:

$$\eta_{\text{creep}} = \left(\frac{1}{\eta_{\text{diff}}} + \frac{1}{\eta_{\text{disl}}}\right)^{-1} \tag{S8}$$

This formulation is derived by assuming that strain rates are additive.

$$\dot{\varepsilon}_{\text{II}} = \dot{\varepsilon}_{\text{diff}} + \dot{\varepsilon}_{\text{disl}} \tag{S9}$$

under the condition of a single deviatoric stress σ

$$\sigma = 2\,\eta_{\text{creep}}\dot{\varepsilon}_{\text{II}} \;=\; 2\,\eta_{\text{diff}}\,\dot{\varepsilon}_{\text{diff}} \;=\; 2\,\eta_{\text{disl}}\,\dot{\varepsilon}_{\text{disl}} \tag{S10}$$

We implement the following iterative procedure to ensure that the dislocation creep viscosity η_{disl} is consistently evaluated using the dislocation creep strain rate $\dot{\varepsilon}_{\text{disl}}$. Indeed only a total creep strain rate is computed from the velocity field, and used to estimate η_{creep}. Deformation partitioning between the two creep mechanisms (diffusion and dislocation) has to be computed iteratively (convergence within a few iterations - we thus enforce 20 iterations in our simulations). This iterative procedure is initialized by computing the dislocation creep viscosity from the total creep strain rate, $\eta^0_{\text{disl}} = \eta_{\text{disl}}(\dot{\varepsilon}_{\text{II}}, T)$ and the creep viscosity following eq. S8 as $\eta^0_{\text{creep}} = \left(\frac{1}{\eta_{\text{diff}}} + \frac{1}{\eta^0_{\text{disl}}}\right)^{-1}$ with $\eta_{\text{diff}} = \eta_{\text{diff}}(T, z)$. For the next iteration steps ($j \geq 1$), the assumption of a single stress (eq. S10) is used to iterate the dislocation creep strain rate as:

$$\dot{\varepsilon}^j_{\text{disl}} \;=\; \dot{\varepsilon}_{\text{II}}\,\frac{\eta^{j-1}_{\text{creep}}}{\eta^{j-1}_{\text{disl}}} \tag{S11}$$

which is used to compute the dislocation creep viscosity as $\eta^j_{\text{disl}} = \eta_{\text{disl}}(\dot{\varepsilon}^j_{\text{disl}}, T)$. We then calculate a new effective creep viscosity as:

$$\eta^j_{\text{creep}} \;=\; \left(\frac{1}{\eta_{\text{diff}}} + \frac{1}{\eta^j_{\text{disl}}}\right)^{-1} \tag{S12}$$

Finally, the amount of strain rate accommodated by dislocation creep is the ratio between $\dot{\varepsilon}_{\text{disl}}$ and $\dot{\varepsilon}_{\text{II}} = \dot{\varepsilon}_{\text{diff}} + \dot{\varepsilon}_{\text{disl}}$ which, because of the condition of a single deviatoric stress, also corresponds to the ratio between the total creep viscosity and the dislocation creep viscosity :

$$\frac{\dot{\varepsilon}_{\text{disl}}}{\dot{\varepsilon}_{\text{creep}}} = \frac{\dot{\varepsilon}_{\text{disl}}}{\dot{\varepsilon}_{\text{diff}} + \dot{\varepsilon}_{\text{disl}}} = 1 - \frac{\dot{\varepsilon}_{\text{diff}}}{\dot{\varepsilon}_{\text{II}}} = \frac{\eta_{\text{II}}}{\eta_{\text{disl}}} \tag{S13}$$

S3.3 Comparison of low-to-high temperature dislocation creep parameterisations

Figure S10 compares stress and viscosity profiles for various parameterizations of LT and HT dislocation creep in olivine derived from experimental data, and often parameterized using the exponential law proposed by Frost and Ashby (1982). Diffusion creep and HT and LT-HT dislocation creep laws used in our study are both comparable at high-temperatures (T > 1100 K, red lines in Fig. S10). The stress and viscosity variation with depth of our LT-HT dislocation creep (Eq. 3 in the main text) falls within the range of other low-temperature plasticity flow laws (for temperatures bellow 1100 K).

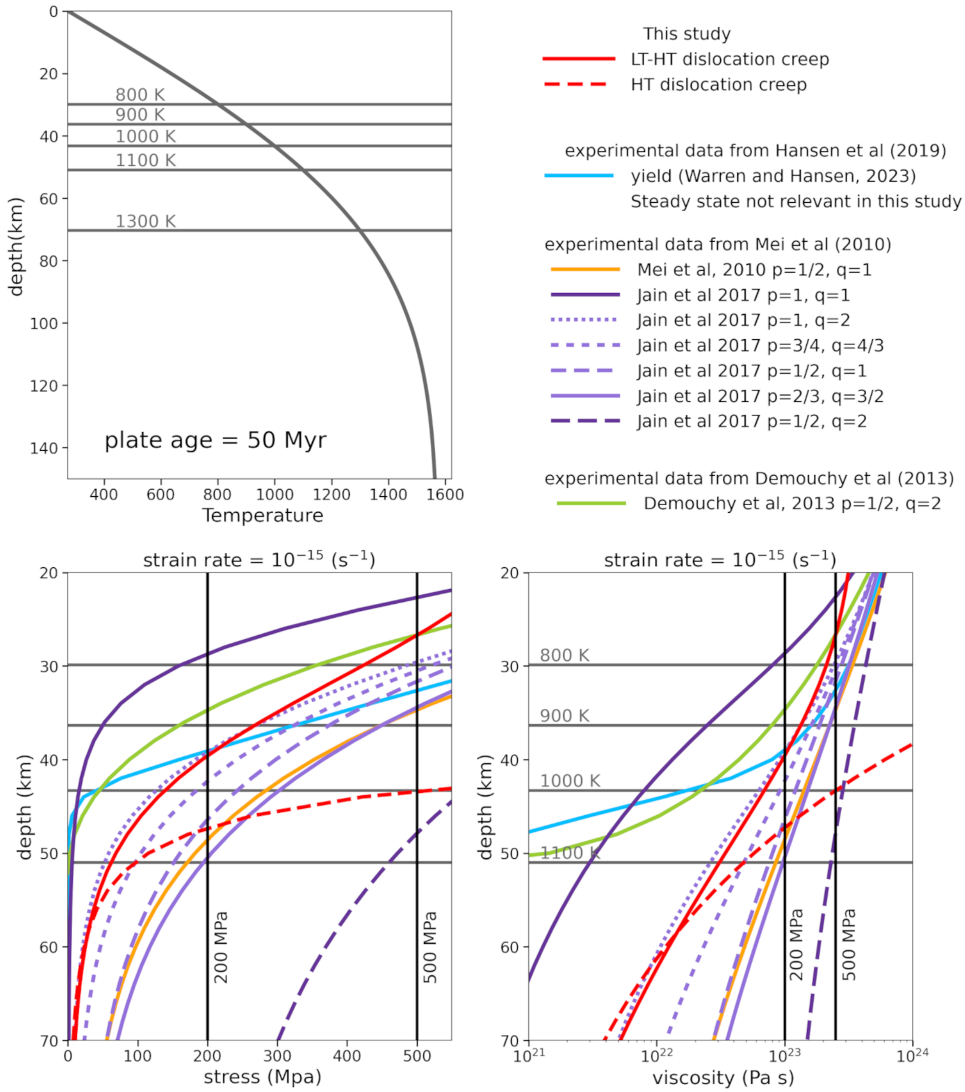

Figure S10. Stress and viscosity vertical profiles between 20 and 70 km depth for a 50 Myr old plate (geotherm calculated for a half-space cooling model with mantle and surface temperatures of 1573 and 273 K, respectively). The profiles are calculated for the parameterization of LT and LT-HT dislocation creep used in our this study, and compared to the following flow laws constrained from deformation experiments. (i) Data from Mei et al. (2010) and Demouchy et al. (2013), acquired at at strain rates around 10^{-5} s^{-1}, extrapolate the semi-empirical exponential law to 10^{-15} s^{-1}. The low-plasticity curve (light blue) corresponds to yielding at the onset of deformation prior to strain hardening (Warren and Hansen, 2023). The 500 and 200 MPa are the yield stress used in this study, with corresponding viscosities shown as black lines. All stress curves are shown below the brittle-plastic transition defined by the Goetze criterion (Kohlstedt et al., 1995).

S4 Diagnostics

S4.1 Details on plateness P calculation

Plateness is a measure of how much surface deformation is spatially localized in narrow boundaries (Tackley, 2000), defined as :

$$P = 1 - \frac{f_{80}}{f_c} \tag{S14}$$

where f_c is the characteristic surface-area fraction for a flow with given vigour and heating mode (Crameri, 2018) (f_c = 1 in this study, as in Fuchs and Becker (2019)) and f_{80} is the relative fraction of the total surface (or distance) in which 80 % of the cumulative deformation occurs (see Fig. S11, for 2-D calculation using relative distance).

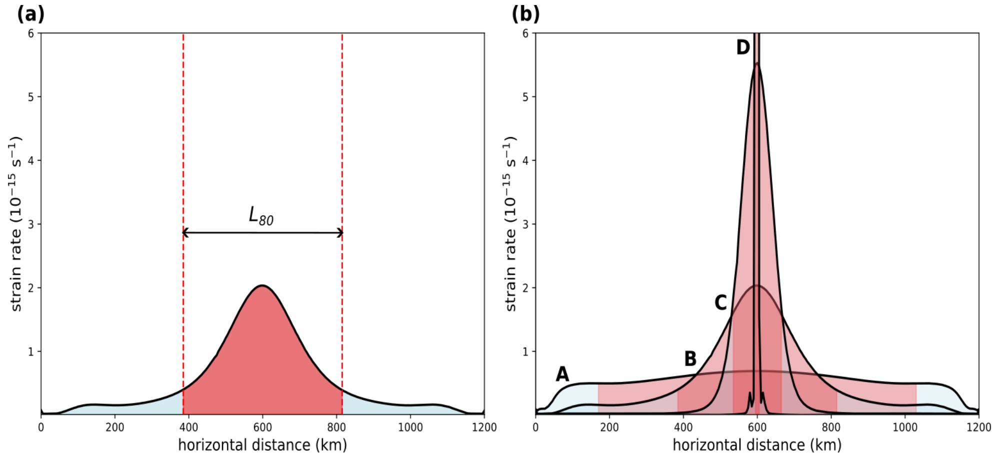

Figure S11. (a) Calculation of plateness P: lateral profile of the strain rate second invariant at the box surface in Simulation ***ref-1*** at 5 Myr. The cumulative deformation is represented by the sum of grey and red areas. L_{80} is the distance over which the 80 % of the cumulative deformation occurs (red area). Fraction $f_{80} = L_{80}/L$, where L is the width of the simulation box (1200 km). **(b)** Strain rate lateral profiles at times 1 Myr (A) - resp. 5 Myr, t_{tr} ∼6.5 Myr (C), t_{PB} ∼12 Myr (D) - associated with peak of strain rate of 0.67·10^{-15}, 2.0·10^{-15}, 5.5·10^{-15} and 117·10^{-15} s^{-1}, respectively; and fraction f_{80} of 0.72, 0.36, 0.11 and 0.01, respectively.

S4.2 Lateral variation of tectonic force TF

The tectonic force is related to the traction acting on the vertical boundary (e.g. Brune et al., 2012). However - probably caused by the 1-D Couette profile - the tectonic force is not relevant when we calculated it too close from a side (Fig. S12). Thus, we chose to calculate the tectonic force 100 km away from the sides.

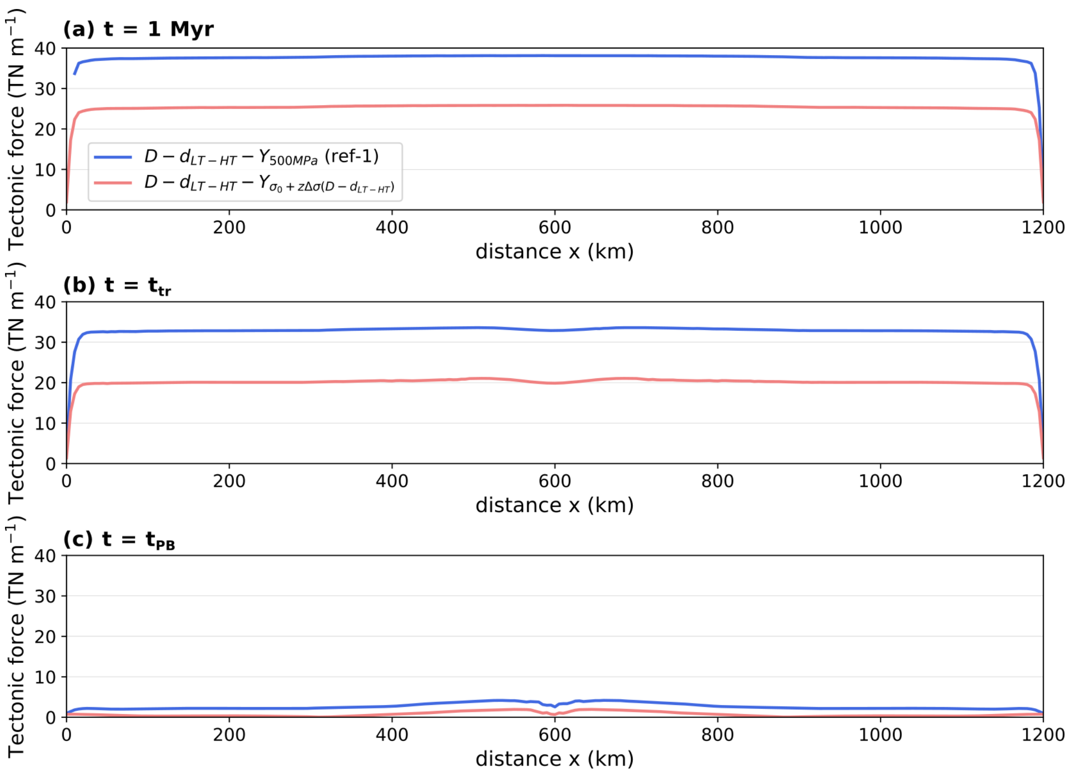

Figure S12. Tectonic force along x axis, for $D - d_{LT-HT}$ creep rheology in combination with constant yield stress of 500 MPa (*Ref-1* simulation, blue) model and depth- dependent yield stress (red), at (a) t = 1 Myr, (b) t = t_{tr} (c) t = t_{PB}.

S5 Additional outputs for discussion

S5.1 Additional simulations with time-dependent extension rate

We perform supplementary simulations with rheology $D - d_{LT-HT} - Y_{500\,\mathrm{MPa}}$, in which the kinematics boundary condition imposed along the vertical sides evolves with time. The half-extension rate $v_{1/2}$ increases following : (i) a linear increase from 0 to 2 cm yr^{-1} over 15 Myr; or an abrupt acceleration (Figure S13a) as in numerical models performed with constant force boundary conditions of (ii) Heine and Brune (2014) or (iii) Brune et al. (2016). The tectonic force TF is roughly

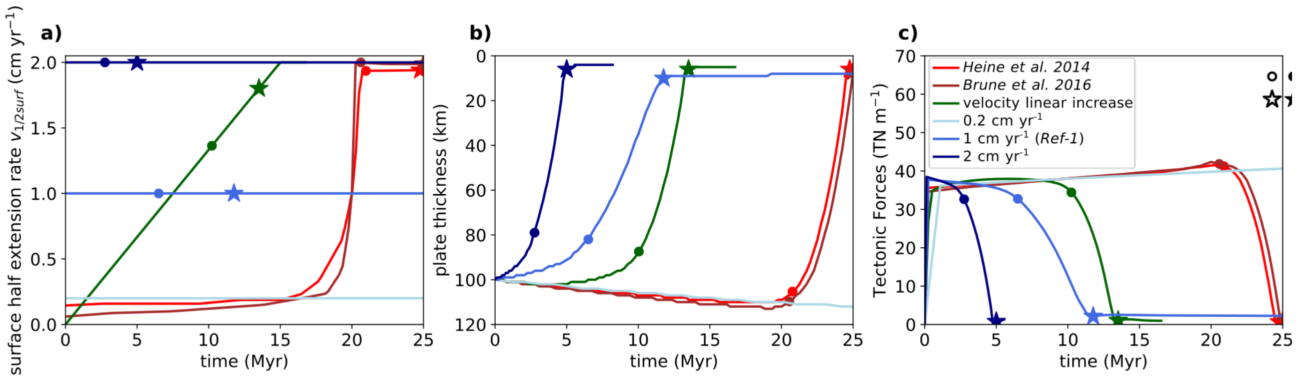

Figure S13. Time evolution of (a) prescribed surface horizontal velocity ($v_{1/2}$) (b) plate thickness h_{plate} at x = 600 km, and (c) tectonic forces TF. Simulations have the same rheology ($D - d_{LT-HT} - Y_{500MPa}$) and initial plate age (50 Myr), but are computed using different extension rates $v_{1/2}$, the latter being either constant, or time-dependent (panel 'a') following a linear increase with time or a time evolutions from Heine and Brune (2014) or Brune et al. (2016). The times t_{tr} and t_{PB} are denoted by points and stars, respectively.

constant during Stage 1 for simulations where the extension velocity is varying with time (Fig. S13c), with Stage 2 is delayed compared to simulations with constant $v_{1/2}$ (Fig. S13). For all simulations featuring an increase of extension rate with time, the upwelling rate is low during Stage 1, equivalent to the simulation at low constant velocity $v_{1/2} = 0.2$ cm yr^{-1}, then increases during Stage 2 to higher values, that are similar to the velocity $v_{1/2} = 2$ cm yr^{-1} imposed in some of our simulation (Fig. S13b). The simulation featuring a velocity linear increase exhibits an homogeneous deformation throughout the whole plate during early stage 1 and then narrows rapidly (Fig. S14a). At the center of the domain, the relative contribution to weakening remains mechanically-dominated during Stage 1 ($F_{\mathrm{SR}} > 60$ %) and thermally-driven during Stage 2 ($F_{\mathrm{T}} > 80$ %) as for $D - d_{LT-HT} - Y_{500\,\mathrm{MPa}}$ rheology featuring steady velocities (compare Figure 8 in the main text to Fig. S14b).

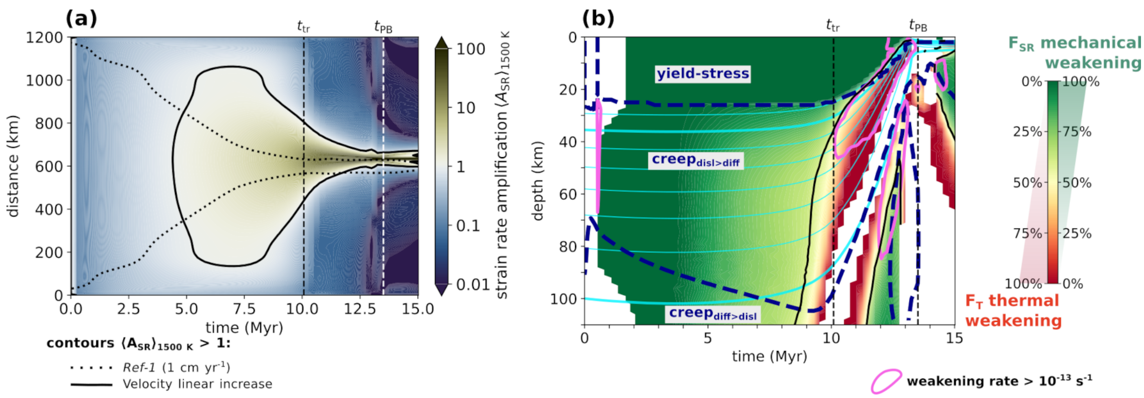

Figure S14. Linear increase with time simulation (see green curve, Fig. S13a). (a) Time-space evolution of the strain-rate amplification $\langle A_{\text{SR}} \rangle_{1500\ \text{K}}(x,t)$, computed as the vertically-averaged ratio relative to a reference strain rate (here $\dot{\varepsilon}_{t_0}$ ~3.73 10^{-16} s^{-1}). Along the black thick line, this ratio is equal to 1, the dashed black line is correspond to ref-1 simulation contour (constant $v_{1/2} = 1\text{cm yr}^{-1}$. (b) Depth-time evolution of the relative contributions to weakening from strain rate (F_{SR}) and temperature (F_T). The diagnostics are only computed for regions in weakening ($W > 0$), with hardening or stable regions shown in white ($W < 0$), and the color scale is capped between 0 and 1. A highly-weakening zone, where the weakening rate normalized 10^{-13} s^{-1}, is highlighted by pink contours. Boundaries between dominant deformation mechanisms are indicated by dashed dark-blue lines, and isotherms from 800 to 1500 K are displayed in light blue.

S5.2 Lateral variations of free-surface topography and of shallow stresses

Free-surface topography evolves with strain localization. For Simulation *ref-1*, the topography at time t_{PB} reaches a maximum of 1.5 km high and minimum of 6.1 km deep at the plate boundary location (Fig. S15). The topography obtained in the extra simulation including a depth-dependent yield stress does not exceed a 2.1 km-deep subsidence. In addition, shallow stresses measured at 5 km depth are high and reach 500 MPa in Simulation *ref-1* compared to a depth-dependent yield stress case for which stresses are reduced to ∼110 MPa (decrease by a factor ~ 4.5), except in the plate boundary area at the very end of the experiment, where the yield stress is reached (Fig. S16). Combining these two results suggests how shallow stresses can influence the free-surface topography: the higher the shallow stresses are, the more pronounced the topography becomes. Since elasticity is neglected in our models, shallow stresses are probably overestimated in our study (e.g. Patocka et al. 2019). However, Simulation *ref-1* and the supplementary simulation performed with a depth-dependent yield stress exhibit the same two-stage scenario of plate weakening and strain localization, the timing of incipient plate boundary formation being very close (see Appendix E in the main text) despite large differences in shallow stresses (Fig. S16). Hence, we conclude that the main results obtained in this study, basically relying on the two-stage weakening of the lithosphere, are expected to remain robust even if stresses may be overestimated in the shallow part of the lithosphere. Nevertheless, we acknowledge that a more realistic simulation of surface processes, including elasticity, would be necessary to focus on an accurate modeling of surface deformation, which is beyond the scope of the present study.

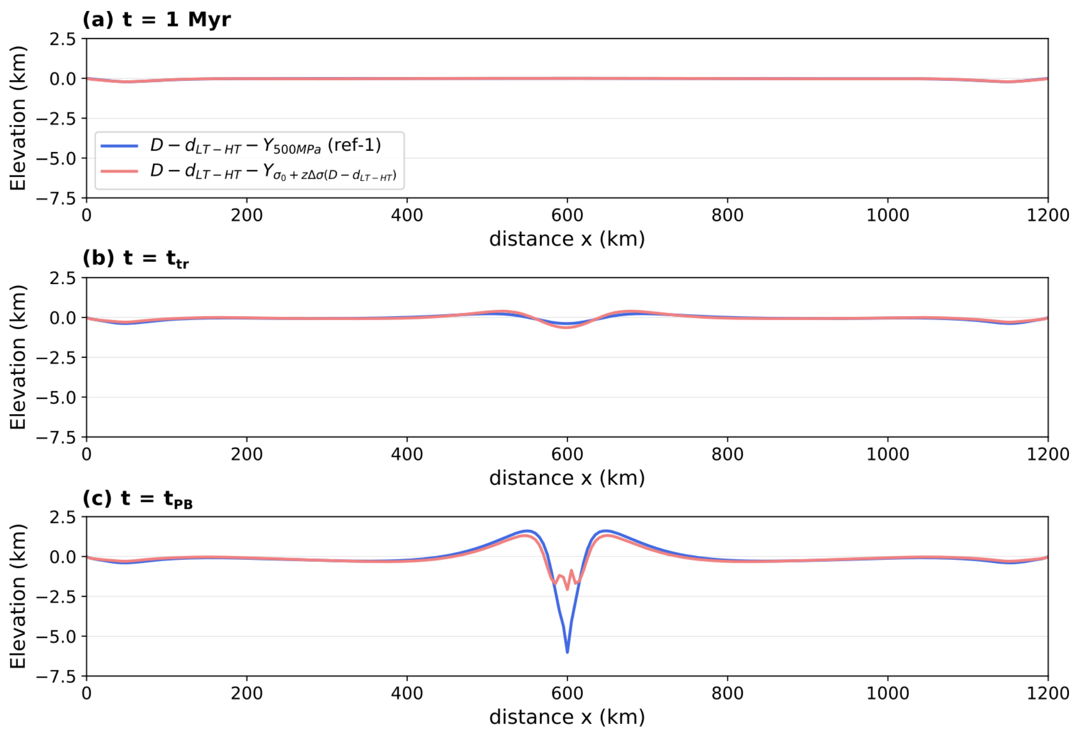

Figure S15. Free-surface topography plotted along the box bottom (x axis), modeled for creep rheology $D - d_{LT-HT}$ in combination with either a constant yield stress of 500 MPa (Simulation *Ref-1*, blue) or a depth-dependent yield stress (red), at (a) t = 1 Myr, (b) t = t_{tr} (c) t = t_{PB}.

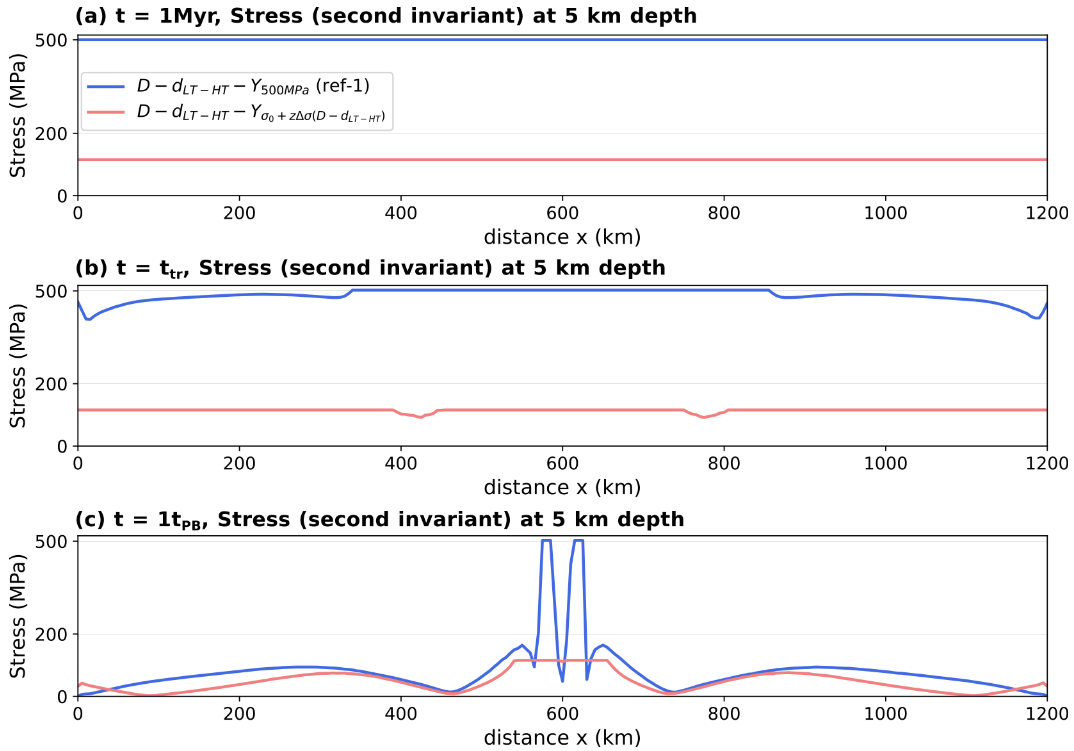

Figure S16. Shallow stresses at 5 km depth displayed along the box top, modeled for creep rheology $D - d_{LT-HT}$ in combination with either a constant yield stress of 500 MPa (Simulation *Ref-1*, blue) or a depth- dependent yield stress (red), at (a) t = 1 Myr, (b) t = t_{tr} (c) t = t_{PB}.

S5.3 Estimate of heat dissipation rate within the creeping lithosphere

We do not include shear heating in our experiments. In order to evaluate its possible effect, we estimate *a posteriori* the heat dissipation rate, $Q = 2 \cdot \sigma_{II} \cdot \dot{\varepsilon}_{II}$, which is predicted to be released mainly in the lithosphere at domain center where deformation is the highest. For Simulation *ref-1* ($D - d_{LT-HT} - Y_{500MPa}$ including low- to high-temperature dislocation creep), we predict a temporal narrowing of the region where this shear heating would be the highest, along with the focusing ot he central deformed zone. Heat dissipation rates larger than 10^{-6} W m^{-3} are reached at t_{tr} for a large zone, and then localized at the plate boundary at t_{PB} (Fig. S17). At time t_{tr}, heat dissipation rate greater than 10^{-6} W m^{-3} expands in a $\sim$15 km thick layer just underneath the yield-creep transition. If the shallow part of the lithosphere undergoing yield stresses cannot be weakened by a temperature increase due to heat dissipation, one may however assume that shear heating could (moderately) lower the creep viscosity through temperature increase, hence rising the transition between yield and creep deformation and expanding the lithosphere domain able to weakn thermally.

Shear heating at time t_{tr} is predicted to b low if only diffusion creep is implemented as creep rheology, located only in the yielding region, and close to zero in the creeping lithosphere (Fig. S18-c). If HT-dislocation creep is considered, the creeping lithospheric layer where thermal weakening is likely to be enhanced by shear heating is estimated to be very thin ($\lesssim$4 km thick, Fig. S18-b).

Finally, we estimate the shear heating amount at time t_{tr} for variable extension rates (Fig. S19). Increasing the spreading velocity increases both the area where heat dissipation rate is predicted to be significant, and also its maximum value. In particular, the higher the extension velocity, the deeper the shear heating likely to be dissipated (Fig. S19-c).

In subduction modeling, heat dissipation $Q > 10^{-5}$ W m^{-3} is associated to a temperature increase slightly greater than 50 °C (e.g. Arcay et al., 2023), in experiments accounting for high-temperature dislocation creep power laws for the creeping mantle. Kiss et al. (2020) observed a greater resulting temperature increase in the shear zone ($\Delta T > 50$ °C) when including low-temperature plasticity. The theoretical heat dissipation rate calculated for our simulations is lower by one order of magnitude. We thus estimate that the resulting temperature increase ΔT will probably be less than 50 K, which would emphasize thermal weakening in the creeping lithosphere, but only mildly. This effect is likely to be the strongest if a low- to high-temperature dislocation creep is simulated, since the low-temperature dislocation creep regime leads to thicker creeping lithosphere, the latter featuring a temperature-dependent viscosity. As a result, shear heating could amplify the weakening feedbacks identified in this paper (see Discussion 5.2 in the main text).

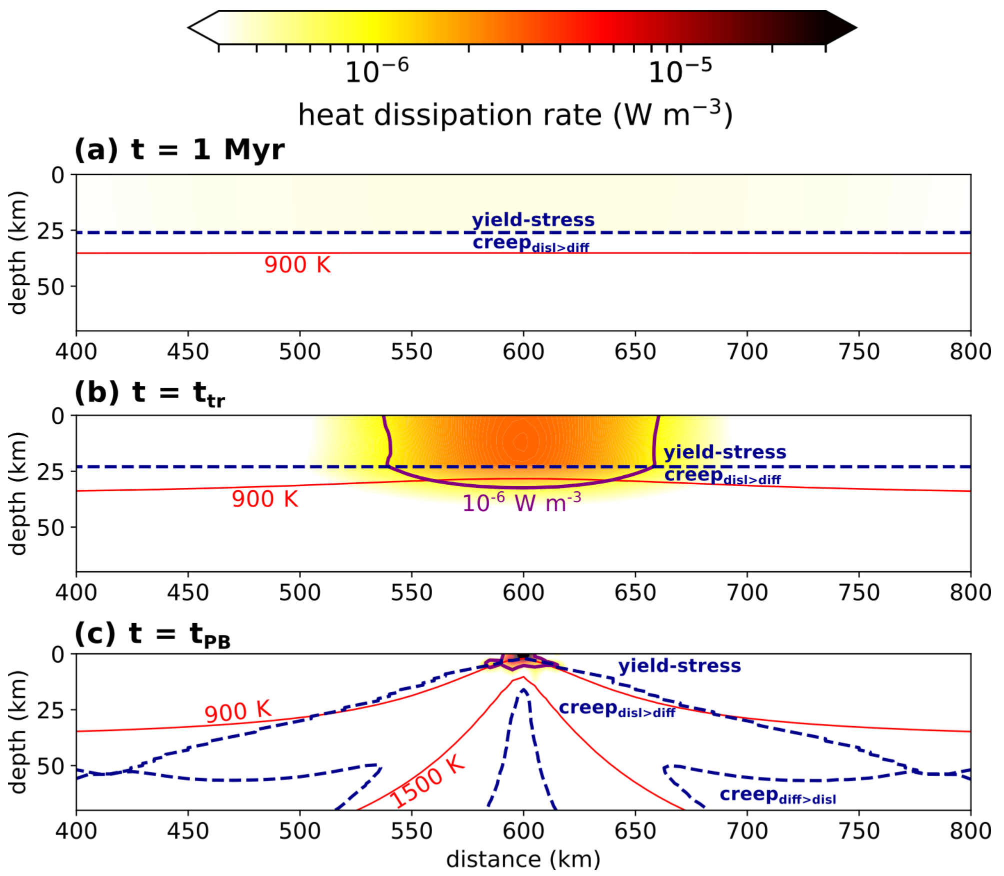

Figure S17. *A posteriori* calculations of the heat dissipation rate in Simulation *ref-1* ($D - d_{LT-HT} - Y_{500MPa}$), at different times: (a) 1 Myr, (b) t_{tr}, (c) t_{PB}. The 900 and 1500 K isotherms are displayed as red lines. The dashed dark blue lines delimit the dominant deformation mechanism. The violet contour highlights the region where the heat dissipation rate exceeds 10^{-6} W m^{-3}. The displayed area corresponds to the x-range from 400 to 800 km and to depths encompassed between the surface and 80 km depth.

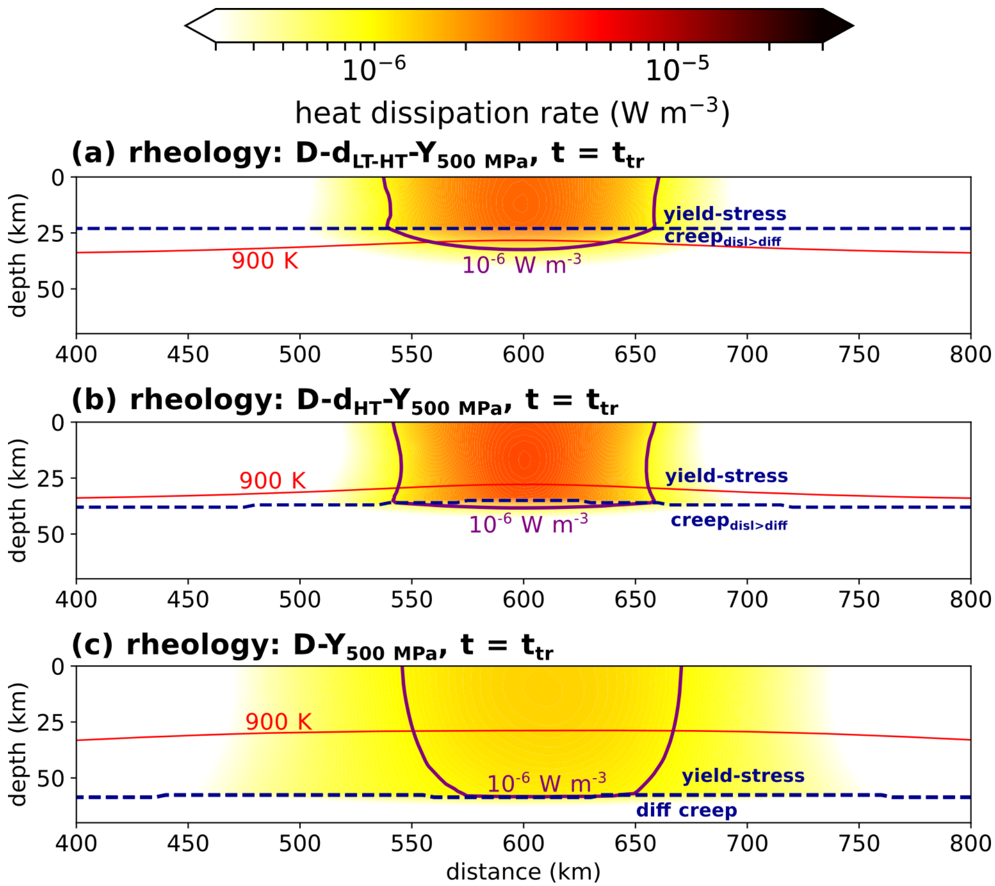

Figure S18. *A posteriori* calculation of the heat dissipation rate at t_{tr} for simulations with three different mantle rheologies: (a) $D - d_{LT-HT} - Y_{500MPa}$, (b) $D - d_{HT} - Y_{500MPa}$, (c) $D - Y_{500MPa}$. The 900 and 1500 K isotherms are displayed as red lines. The dashed dark blue lines delimit the dominant deformation mechanism. The violet contour highlights the region where the heat dissipation rate exceeds 10^{-6} W m^{-3}. The displayed area corresponds to the x-range from 400 to 800 km and to depths encompassed between the surface and 80 km depth.

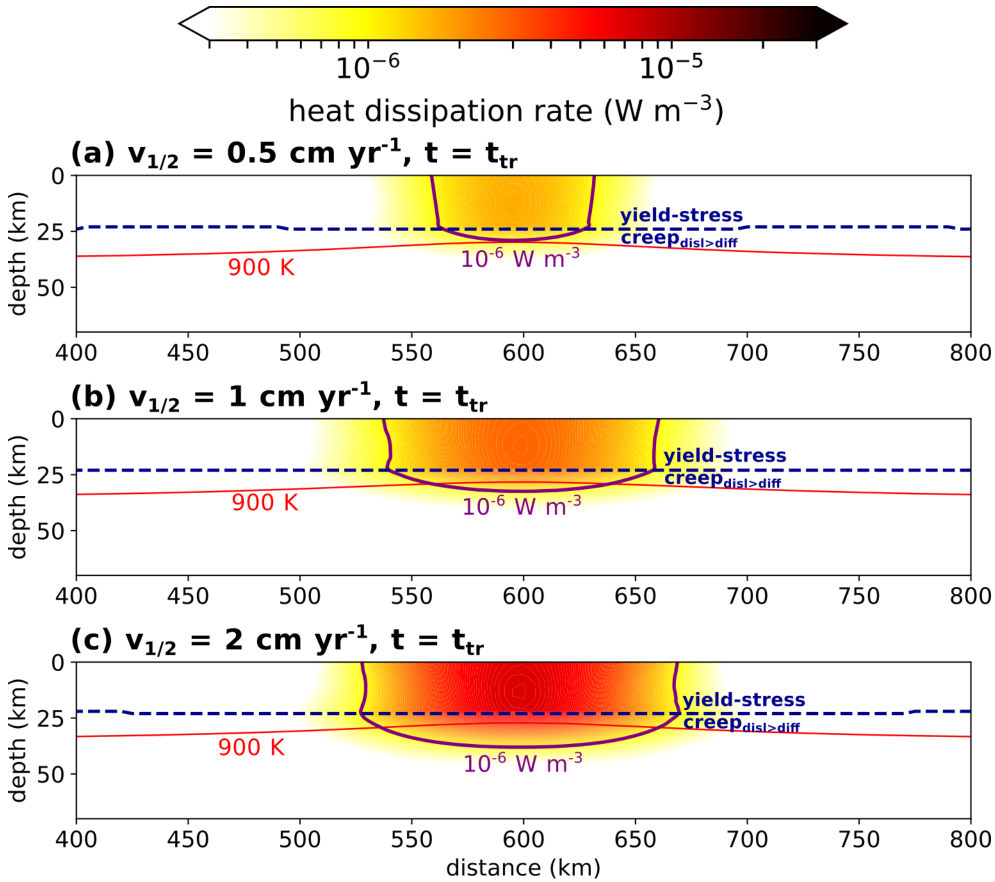

Figure S19. *A posteriori* calculations of the heat dissipation rate at time t_{tr} of simulations performed with rheology $D{-}d_{LT-HT}{-}Y_{500MPa}$, for different extension rates $v_{1/2}$ (close-up on the area delimited in x rom 400 to 800 km and in z from 0 to 80 km): (a) 0.5 cm yr^{-1} , (b) 1 cm yr^{-1} (*ref-1*), (c) 2 cm yr^{-1}. The 900 and 1500 K isotherms are displayed as red lines. The dashed dark blue lines delimit the dominant deformation mechanism. The violet contour highlights the region where the heat dissipation rate exceeds 10^{-6} W m^{-3}.

References

Arcay, D., Abecassis, S., and Lallemand, S.: Subduction initiation at an oceanic transform fault experiencing compression: Role of the fault structure and of the brittle-ductile transition depth, Earth and Planetary Science Letters, 618, 118 272, https://doi.org/10.1016/j.epsl.2023.118272, 2023.

Brune, S., Popov, A. A., and Sobolev, S. V.: Modeling suggests that oblique extension facilitates rifting and continental break-up, Journal of Geophysical Research: Solid Earth, 117, https://doi.org/10.1029/2011JB008860, publisher: John Wiley & Sons, Ltd, 2012.

Brune, S., Williams, S. E., Butterworth, N. P., and Müller, R. D.: Abrupt plate accelerations shape rifted continental margins, Nature, 536, 201–204, https://doi.org/10.1038/nature18319, publisher: Nature Publishing Group, 2016.

Crameri, F.: Geodynamic diagnostics, scientific visualisation and StagLab 3.0, Geoscientific Model Development, 11, 2541–2562, https://doi.org/10.5194/gmd-11-2541-2018, 2018.

Demouchy, S., Tommasi, A., Ballaran, T. B., and Cordier, P.: Low strength of Earth's uppermost mantle inferred from tri-axial deformation experiments on dry olivine crystals, Physics of the Earth and Planetary Interiors, 220, 37–49, publisher: Elsevier, 2013.

Frost, H. J. and Ashby, M. F.: Deformation mechanism maps: the plasticity and creep of metals and ceramics, Pergamon press, 1982.

Fuchs, L. and Becker, T. W.: Role of strain-dependent weakening memory on the style of mantle convection and plate boundary stability, Geophysical Journal International, 218, 601–618, publisher: Oxford University Press, 2019.

Garel, F. and Thoraval, C.: Lithosphere as a constant-velocity plate: Chasing a dynamical LAB in a homogeneous mantle material, Physics of the Earth and Planetary Interiors, p. 106710, publisher: Elsevier, 2021.

Heckenbach, E. L., Brune, S., Glerum, A. C., and Bott, J.: Is There a Speed Limit for the Thermal Steady-State Assumption in Continental Rifts?, Geochemistry, Geophysics, Geosystems, 22, e2020GC009 577, https://doi.org/10.1029/2020GC009577, _eprint: https://onlinelibrary.wiley.com/doi/pdf/10.1029/2020GC009577, 2021.

Heine, C. and Brune, S.: Oblique rifting of the Equatorial Atlantic: Why there is no Saharan Atlantic Ocean, Geology, 42, 211–214, https://doi.org/10.1130/G35082.1, 2014.

Huismans, R. S. and Beaumont, C.: Roles of lithospheric strain softening and heterogeneity in determining the geometry of rifts and continental margins, Geological Society, London, Special Publications, 282, 111–138, https://doi.org/10.1144/SP282.6, publisher: The Geological Society of London, 2007.

Kiss, D., Candioti, L. G., Duretz, T., and Schmalholz, S. M.: Thermal softening induced subduction initiation at a passive margin, Geophysical Journal International, 220, 2068–2073, https://doi.org/10.1093/gji/ggz572, 2020.

Kohlstedt, D. L., Evans, B., and Mackwell, S. J.: Strength of the lithosphere: Constraints imposed by laboratory experiments, Journal of Geophysical Research: Solid Earth, 100, 17 587–17 602, https://doi.org/10.1029/95JB01460, _eprint: https://onlinelibrary.wiley.com/doi/pdf/10.1029/95JB01460, 1995.

Mei, S., Suzuki, A., Kohlstedt, D., Dixon, N., and Durham, W.: Experimental constraints on the strength of the lithospheric mantle, jgr, 115, B08 204, https://doi.org/10.1029/2009JB006873, 2010.

Patočka, V., Čížková, H., and Pokorný, J.: Dynamic Component of the Asthenosphere: Lateral Viscosity Variations Due To Dislocation Creep at the Base of Oceanic Plates, Geophysical Research Letters, 51, e2024GL109 116, https://doi.org/10.1029/2024GL109116, _eprint: https://agupubs.onlinelibrary.wiley.com/doi/pdf/10.1029/2024GL109116, 2024.

Tackley, P. J.: Self-consistent generation of tectonic plates in time-dependent, three-dimensional mantle convection simulations 1 Pseudoplastic yielding, Geochemistry, Geophysics, Geosystems, 1, https://doi.org/10.1029/2000GC000036, _eprint: https://onlinelibrary.wiley.com/doi/pdf/10.1029/2000GC000036, 2000.

Tetreault, J. L. and Buiter, S. J. H.: The influence of extension rate and crustal rheology on the evolution of passive margins from rifting to break-up, Tectonophysics, 746, 155–172, https://doi.org/10.1016/j.tecto.2017.08.029, 2018.

Warren, J. M. and Hansen, L. N.: Ductile deformation of the lithospheric mantle, Annual Review of Earth and Planetary Sciences, 51, 581–609, 2023.